nature biotechnology

Minimally invasive endovascular stent-electrode array for high-fidelity, chronic recordings of cortical neural activity

Thomas J Oxley[1–4], Nicholas L Opie[1–4], Sam E John[1–4], Gil S Rind[1–3], Stephen M Ronayne[1–3], Tracey L Wheeler[5], Jack W Judy[6], Alan J McDonald[3], Anthony Dornom[3], Timothy J H Lovell[1–3], Christopher Steward[2,7,8], David J Garrett[9,10], Bradford A Moffat[7,8,11], Elaine H Lui[7,8], Nawaf Yassi[2], Bruce C V Campbell[2], Yan T Wong[1,4], Kate E Fox[9,12], Ewan S Nurse[1,4], Iwan E Bennett[13], Sébastien H Bauquier[14], Kishan A Liyanage[1], Nicole R van der Nagel[1], Piero Perucca[2], Arman Ahnood[9], Katherine P Gill[1], Bernard Yan[2], Leonid Churilov[3,15], Christopher R French[2], Patricia M Desmond[7,8], Malcolm K Horne[3], Lynette Kiers[2], Steven Prawer[9], Stephen M Davis[2], Anthony N Burkitt[4,10], Peter J Mitchell[7,8], David B Grayden[1,4,10,16], Clive N May[1,3] & Terence J O'Brien[2]

High-fidelity intracranial electrode arrays for recording and stimulating brain activity have facilitated major advances in the treatment of neurological conditions over the past decade. Traditional arrays require direct implantation into the brain via open craniotomy, which can lead to inflammatory tissue responses, necessitating development of minimally invasive approaches that avoid brain trauma. Here we demonstrate the feasibility of chronically recording brain activity from within a vein using a passive stent-electrode recording array (stentrode). We achieved implantation into a superficial cortical vein overlying the motor cortex via catheter angiography and demonstrate neural recordings in freely moving sheep for up to 190 d. Spectral content and bandwidth of vascular electrocorticography were comparable to those of recordings from epidural surface arrays. Venous internal lumen patency was maintained for the duration of implantation. Stentrodes may have wide ranging applications as a neural interface for treatment of a range of neurological conditions.

© 2016 Nature America, Inc. All rights reserved.

Engineering and medicine continue to converge in the field of bionics, which is transforming therapeutic approaches for many indications. Neural bionic devices aim to electronically substitute damaged nerves or neurons to overcome failed information processing. Initially focused on stimulation technologies, this rapidly growing field has had a profound impact not only on the treatment of various neurological conditions, including movement disorders[1] and psychological conditions[2] but also on the development of devices that restore hearing[3] and sight[4]. Recently, advances in chronic neural recording devices have facilitated learned, willful control of robotic prosthetic limbs for the treatment of paralysis[5] and have improved seizure prediction with chronic telemetry in refractory epilepsy[6,7]. Intracranial electrode arrays, such as penetrating cortical microelectrodes[8] and subdural electrode arrays, have enabled neural recording and decoding for complex motor prostheses and epilepsy seizure monitoring[6,7,9,10]. Although penetrating cortical arrays have achieved the highest spatial resolution for neural recordings, they are invasive, may cause trauma to brain tissue during insertion, and may result in chronic inflammation, gliosis and disruption of the blood-brain barrier[11–13]. Furthermore, existing cortical implant design and implantation procedures are associated with difficulty in accessing deep cortical regions, such as within sulcal folds, which may be information-rich regions[14]. Therefore, there is a need for interfaces with improved biocompatibility, high-resolution signal transduction and long-term functionality that can be implanted with minimal trauma.

Cerebral veins naturally lie in sulcal folds and may represent an avenue to deliver minimally invasive cortical interfaces. Since the first report in 1969 of a transient endovascular recording of brain activity[15], multiple studies have repeated acute recordings over a period of hours during cerebral angiography using wire or catheter electrode probes[16–20]. The clinical utility for an endovascular recording system depends on its ability to achieve long-term recordings in

[1]Vascular Bionics Laboratory, Melbourne Brain Centre, Department of Medicine, The University of Melbourne, Melbourne, Australia. [2]Departments of Medicine and Neurology, Melbourne Brain Centre at The Royal Melbourne Hospital, The University of Melbourne, Melbourne, Australia. [3]The Florey Institute of Neuroscience and Mental Health, The University of Melbourne, Melbourne, Australia. [4]NeuroEngineering Laboratory, Department of Electrical & Electronic Engineering, The University of Melbourne, Melbourne, Australia. [5]Craig H. Neilsen Foundation, Encino, California, USA. [6]Nanoscience Institute for Medical and Engineering Technology, University of Florida, Gainesville, Florida, USA. [7]Department of Radiology, Royal Melbourne Hospital, Melbourne Health, Melbourne, Australia. [8]Department of Radiology, The University of Melbourne, Melbourne, Australia. [9]School of Physics, The University of Melbourne, Melbourne, Australia. [10]The Bionics Institute, East Melbourne, Victoria, Australia. [11]Department of Anatomy and Neuroscience, The University of Melbourne, Melbourne, Australia. [12]Centre for Additive Manufacturing, School of Aerospace, Mechanical and Manufacturing Engineering, RMIT University, Melbourne, Australia. [13]Department of Surgery, Royal Melbourne Hospital, The University of Melbourne, Melbourne, Australia. [14]Translational Research and Clinical Trials (TRACTs), Veterinary Hospital, Faculty of Veterinary and Agricultural Sciences, The University of Melbourne, Melbourne, Australia. [15]School of Mathematics and Geospatial Sciences, RMIT University, Melbourne, Australia. [16]Centre for Neural Engineering, The University of Melbourne, Melbourne, Australia. Correspondence should be addressed to T.J.O. (thomas.oxley@unimelb.edu.au).

Received 18 April 2015; accepted 9 November 2015; published online 8 February 2016; doi:10.1038/nbt.3428

awake and mobile subjects. Long-term deposition of electrodes inside a vein to achieve stimulation and/or recording of local neural tissue has been reported previously in the form of the implantable artificial cardiac pacemaker and defibrillator[21,22]. Intracranial stenting of cerebral blood vessels is an established technique in endovascular neurosurgery for the treatment of both arterial[23] and venous neurological conditions[24], but the capability to record endovascular electrophysiological activity for extended periods of time has not been reported previously to our knowledge.

Here we report a chronically implantable, endovascular device capable of recording intracranial neural activity. We assessed human cortical veins with respect to their proximity to potential recordings sites in sulci and developed a large-animal model to target the sensorimotor cortex. We demonstrate the ability of a self-expanding stent electrode array (stentrode) delivered via catheter angiography to record vascular electrocorticography in awake sheep for up to 190 d. We validated the electrophysiological signals captured with the stentrode by comparing them with those obtained from electrode arrays implanted via craniotomy.

RESULTS

Mapping cerebral veins and cortical surface

To assess the suitability of human cerebral veins as an implant target to record vascular electrocorticography, we focused feasibility studies on the sensorimotor cortex. We specifically focused on the central sulcus as previous work demonstrated the anterior bank of the motor area is information-rich for motor decoding when compared with other areas of motor cortex[14]. We characterized the venous anatomy surrounding the sensorimotor cortex using brain magnetic resonance imaging (MRI) data from 50 patients (**Supplementary Fig. 1**). We identified a network of four venous structures lying in sulci in close proximity to sensorimotor cortex: superior sagittal sinus (SSS), precentral sulcal vein (preCSV), central sulcal vein (CSV) and postcentral sulcal vein (postCSV) (**Supplementary Fig. 2** and **Supplementary Table 1**). The central sulcal vein was closest to the cortical surface, lying immediately adjacent (0 mm, median; 0–4.1 mm, interquartile range; $n = 48$) to the motor area (Brodman Area 4, BA4) at a point along the vein 25 mm distal from the convergence with the SSS (**Fig. 1**). At this point the CSV had a diameter of 3.7 mm (3.4–4.1 mm; $n = 48$). The vein then continued distally, immediately alongside the motor area for a length of 70 mm, reducing in size along the course of the vessel to 2.3 mm (1.8–2.9 mm). Superficial cortical veins displayed some minor anatomical variability in the proximal segments, reflected by reduced concordance of repeated, interobserver and intraobserver measurements of vessel diameters (**Supplementary Fig. 3** and **Supplementary Note 1**).

To find a suitable animal model, we assessed superior sagittal sinus size and position in sheep, as a comparable vessel to the human central sulcal vein, using MRI scans of sheep brains. Sheep SSS lay adjacent to motor cortex, and displayed comparable vessel diameters and proximity to cortical surface (**Fig. 1**). Because the internal luminal diameter of the sheep SSS was 2.4 mm (2.4–2.5 mm, interquartile range; $n = 13$) proximally, reducing to 1 mm (1.0–1.1 mm) distally, we considered it an appropriate venous structure in which to perform validation experiments (**Supplementary Table 2**).

Stentrode delivery

We decided to build our stentrodes on intracranial stent technology currently in clinical use[25,26] to facilitate easy transfer from animal models to humans. We used a commercially available, self-expanding stent (Solitaire SAB, Covidien) as a scaffold for the attachment of 750 μm diameter, laser-cut platinum disc electrodes (**Fig. 2**). To maintain the super-elastic properties of the nitinol stent, we mounted electrodes along the repeating stent strut cross-links 2.5 mm apart (**Supplementary Fig. 4** and **Supplementary Note 2**). The self-expanding scaffold enabled the electrode array to be compressed during minimally invasive delivery via a catheter, and to achieve non-linear expansion to match target vessel curvature for close vessel wall apposition of electrodes against cortical surface after deployment.

To achieve distal access of our stentrode to vessels equal in size to human cortical veins in the sheep model, we used an angiography-based coaxial catheter technique (**Supplementary Fig. 5**) effective at delivering a 4F catheter (DAC044, Stryker Neurovascular) (**Supplementary Tables 3** and **4**) to the sheep target vessel with a diameter of 2 mm. Catheterization of the cerebral venous system was challenged by irregular venous anatomy including valves, chordae and arachnoid granulations[27,28], and we overcame the challenges with specific catheter-over-wire techniques (Online Methods). We implanted the stentrode into the SSS (**Fig. 2**) immediately adjacent to the motor area (Online Methods). We sutured the lead at the common jugular vein puncture site in the neck to achieve hemostasis, tunneled subcutaneously to a custom-made hermetic connector secured to the sternocleidomastoid and exited the skin via a flexible percutaneous lead, which terminated in a microcircular plug (Omnetics).

Vessel wall incorporation

To investigate the process of incorporating the stentrode into the vessel wall, we assessed the strut-to-lumen distance and the change in impedance over the duration of implantation. We measured strut-to-lumen distances *ex vivo* using synchrotron X-ray imaging, which increased with the duration of implantation: on day 1, 21 ± 8 μm (mean ± s.e.m.; $n = 97$ struts in 2 sheep), at three weeks, 309 ± 22 μm ($n = 89$ struts in 4 sheep), and at four months, 320 ± 22 μm ($n = 72$ struts in 4 sheep) (**Supplementary Table 5**). Vessel wall incorporation of the stentrode is a desired outcome with respect to device stability, safety and proximity to target tissue.

Stent incorporation into vessel-wall has been widely reported via the process of endothelialization and neointimal proliferation[29], occurring as quickly as 7 d in arteries[30]. To assess changes at the electrode-tissue interface over the period of implantation, we performed electrochemical impedance spectroscopy on alternate days up to two weeks and weekly thereafter. We observed electrode wires that became short-circuited to the stent wire owing to mechanical fatigue to have 10 kHz impedances below 1 kΩ, and we excluded them from subsequent analysis (**Supplementary Fig. 6** and **Supplementary Note 3**). Low-frequency (<1 kHz) phase and impedance values changed over the course of the first week (**Fig. 3**). We observed a significant effect of the duration of implantation on phase angle at 100 Hz (one-way analysis of variance (ANOVA), $P < 0.0001$). Multiple comparisons (Tukey's test, corrected) revealed this effect to be explained by changes occurring within the first 6 d of implantation, given that we detected no significant effect between days 8 and 28 ($P = 0.619$–0.999). To identify the greatest contributor to the observed changes, we fitted mean electrochemical impedance spectroscopy measurements to an equivalent circuit model (**Supplementary Fig. 7** and **Supplementary Note 4**). The model demonstrated a capacitive increase occurring at the electrode-tissue interface from day 0 (0.167 ± 0.002 μF, mean ± s.d.) to day 28 (4.206 ± 0.102 μF), which may relate to absorption and densification of surface proteins onto the electrode surface[31,32]. These results suggest that vessel-wall incorporation of the stentrode in the sheep SSS had occurred as early as 6 d.

© 2016 Nature America, Inc. All rights reserved.

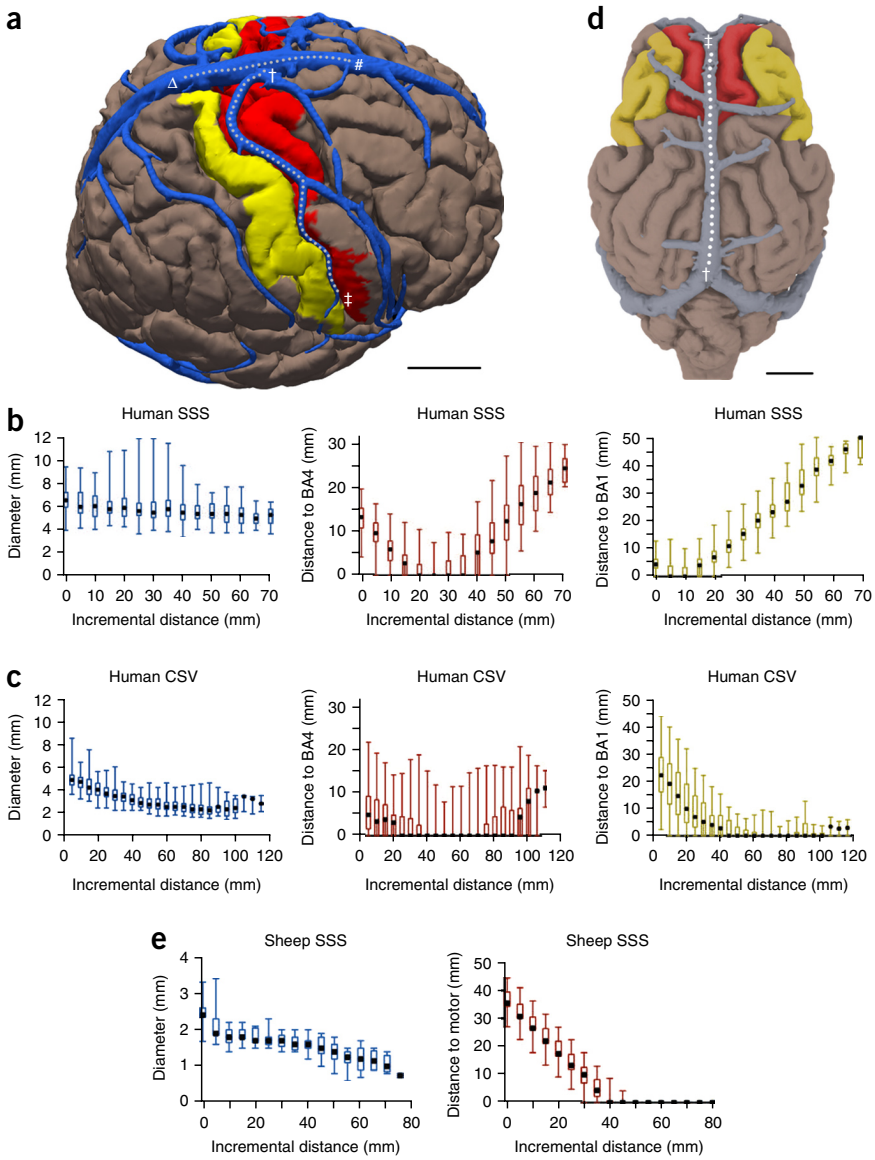

Figure 1 Superficial cortical venous variability in humans and a sheep model. (**a**) Three-dimensional reconstruction of human pial surface, motor cortex (Brodmann area 4 (BA4); red) and sensory cortex (BA1; yellow) with co-registered SSS and CSV. Dotted lines represent segments of vessels characterized at 5-mm increments. Scale bar, 3 cm. (**b**) Incremental diameters and distances (box and whisker plot); median, interquartile range and range of SSS commencing proximally at post-central sulcus (defined as 0 mm in **b**) to nearest BA4 and BA1 cortical surface ($n = 50$). (**c**) Similar values for human CSV, commencing at SSS (defined as 0 mm in **c**) ($n = 50$). (**d**) Three-dimensional reconstruction of sheep SSS and motor (red) and sensory cortex (yellow). Scale bar, 1 cm. (**e**) Sheep SSS diameters and distance to motor area, (box and whisker plot) ($n = 13$).

Vascular electrocorticography

We analyzed endovascular brain signals recorded from the stentrode as functions of both time and electrode location, and validated them against commercially available surface electrocorticography arrays. In sheep, we implanted the strentrode in the distal aspect of the SSS, adjacent to motor cortex in the superior frontal gyrus (**Fig. 4**). We anatomically confirmed stentrode position using pre-implant MRI and post-implant computerized tomography (CT) co-registration. We removed recordings from electrodes short-circuited to the stent by applying common average referencing to viable electrodes only (**Supplementary Fig. 6**). Mechanical failures unrelated to the recording system (**Supplementary Fig. 8**) prevented recording beyond 28 d in this cohort, with three systems confirmed to have fractures of the stent wire in the neck on X-ray, presumed to be related to metal fatigue from the sheep's repeated neck movement. X-ray–measured post-implantation mean electrode pitch on the stent head was 2.38 ± 0.66 mm (mean ± s.d.; $n = 30$).

To assess both the spatial resolution of individual electrodes and their recording stability over time, we used cortically generated somatosensory evoked potentials (SSEPs), elicited from direct electrical stimulation of forelimb (median nerve). We measured SSEPs on freely moving sheep on alternate days for two weeks and weekly up to 28 d. No significant change in peak-to-peak amplitudes was noted over time (random-effect linear regression model, $P = 0.42$, $n = 703$), indicative of stable recordings over the 28 d (**Fig. 4b**).

SSEPs were detectable in 98% of all functional channels (left and right limb stimulation, $n = 64$ channels, $n = 32$ electrodes) over the 28 d. However, the onset of SSEP detection varied over the first few days post-implant. Specifically, the fraction of channels yielding SSEP signals increased from day 1 (50%, median (25–100%, interquartile range); $n = 62$ channels in 5 sheep) to day 2 (79% (62–96%); $n = 44$ channels in 5 sheep) to day 4 (92% (77–100%), $n = 34$ channels in 5 sheep) (**Fig. 4c**). This finding is suggestive of an improvement in recording sensitivity over the first several days of implantation.

We observed variable electrophysiological waveform morphology in individual electrodes. The Pearson's correlation coefficient between electrodes separated by 2.4 mm was 0.06 ± 0.03, significantly reducing to -0.08 ± 0.03 at a separation of 12 mm ($P = 0.028$; Wilcoxon rank-sum test). Phase reversal of SSEP peak amplitudes occurred in 4 of 5 sheep (**Fig. 4**) with dipoles occurring at varying locations adjacent to the motor cortex (**Supplementary Fig. 9**). We also saw this phase reversal in the Pearson's correlation coefficients calculated across all electrode pairs, demonstrated with a significant change in correlation ($P = 0.01$; Wilcoxon rank sum test; **Supplementary Fig. 10**). Detection of SSEP phase reversal in humans is an established method of determining the position of the central sulcus[33], with amplitude disparities reflecting recordings from precentral and postcentral regions on the cortical surface[34]. Although cortical representations of sensorimotor cortex are not separated by an equivalent sulcal pattern in sheep, our results suggest that the signal variability in individual electrodes reflected recordings of neural activity in discrete neuronal populations. Our findings suggest that a spatial resolution of at least 2.4 mm (electrode spacing) is achievable with neural recordings from within a blood vessel wall.

© 2016 Nature America, Inc. All rights reserved.

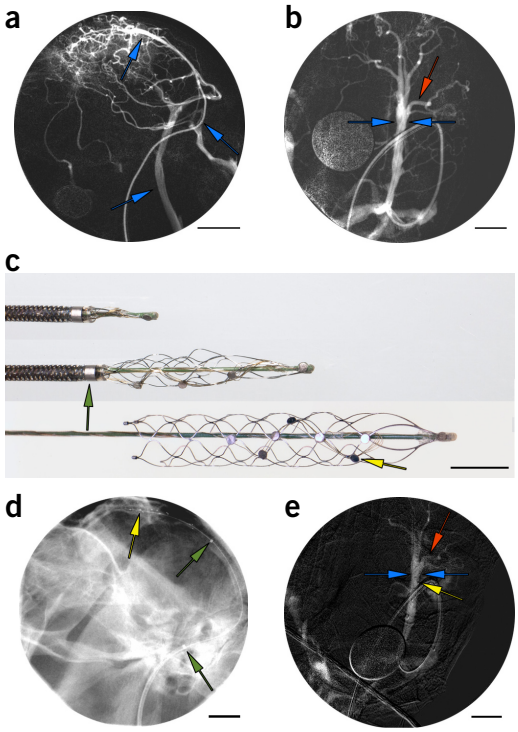

Figure 2 Stentrode delivery. (**a**) Pre-implant lateral projection cerebral venography roadmap of external jugular vein, confluence of sinuses and SSS (blue arrows). Scale bar, 20 mm. Circular artifact is a calibration tool. (**b**) Superior projection of SSS. Lumen diameter (blue arrows) and cortical veins (red arrow), assessed pre and post-implant. Scale bar, 10 mm. (**c**) Stentrode with 8 × 750 µm electrode discs (yellow arrow) self-expanding during deployment from 4F catheter (green arrow). Scale bar, 3 mm. (**d**) Post-implantation lateral projection plain X-ray of stentrode in SSS, displaying electrodes (yellow arrow) and delivery catheters (green arrows). Scale bar, 10 mm. (**e**) Post-implant superior projection contrast study of stentrode (electrodes, yellow arrow). Scale bar, 10 mm.

To assess the effect of post-implantation time on recording sensitivity, we used induction of theta burst-suppression with anaesthesia[35], comparing recordings of neural activity at day 0 versus one month and with light versus deep anesthesia. We found a significant effect of duration of implantation (two-way ANOVA, $F_{1,8} = 12.2$, $P = 0.008$, $n = 5$), with detection of a substantially larger burst-suppression ratio in recordings at one month (0.51 ± 0.07 (mean ± s.e.) when compared with day 0 (0.12 ± 0.05), confirming the effect post-implantation time on stentrode recording quality (**Fig. 5**).

To assess the power spectra and recording bandwidth of the stentrode, we validated recorded signals in acute experiments (n = 41 electrodes in 8 subjects) against contemporaneous recordings of commercially available surface electrocorticography arrays implanted subdurally (2.3-mm diameter discs in 8 × 1 array, n = 25 electrodes in 5 subjects, Ad-Tech Medical), and epidurally (750-µm diameter discs 8 × 2 array, n = 44 electrodes in 3 subjects, CorTec GmbH) via craniotomy (**Supplementary Fig. 11**). Both stentrode and surface electrocorticography (ECoG) array recordings demonstrated a characteristic (1/*f*) frequency-dependent reduction in amplitude (**Fig. 5**). The average normalized power spectra from each sheep showed a difference between the power of subdural recordings and endovascular recordings (two-sided *t*-test $P < 0.001$; **Fig. 5**) but not between the power of epidural and endovascular recordings. Specifically, the amplitudes of subdural ECoG recordings were higher than those of vascular ECoG signals at frequencies below 200 Hz (Lin's concordance coefficient 0.7–0.91; scaling factor 0.61–0.92). However, we found no significant differences between the amplitudes of vascular and epidural ECoG (Lin's concordance coefficient 0.95–0.99; scaling factor 0.85–0.93). In addition, we compared the absolute powers within ECoG bands across all arrays. A one-way ANOVA (Tukey, corrected) revealed frequency-dependent power differences between the stentrode, epidural and subdural recordings. In the mu, beta and lower gamma bands, there were no statistically significant differences

© 2016 Nature America, Inc. All rights reserved.

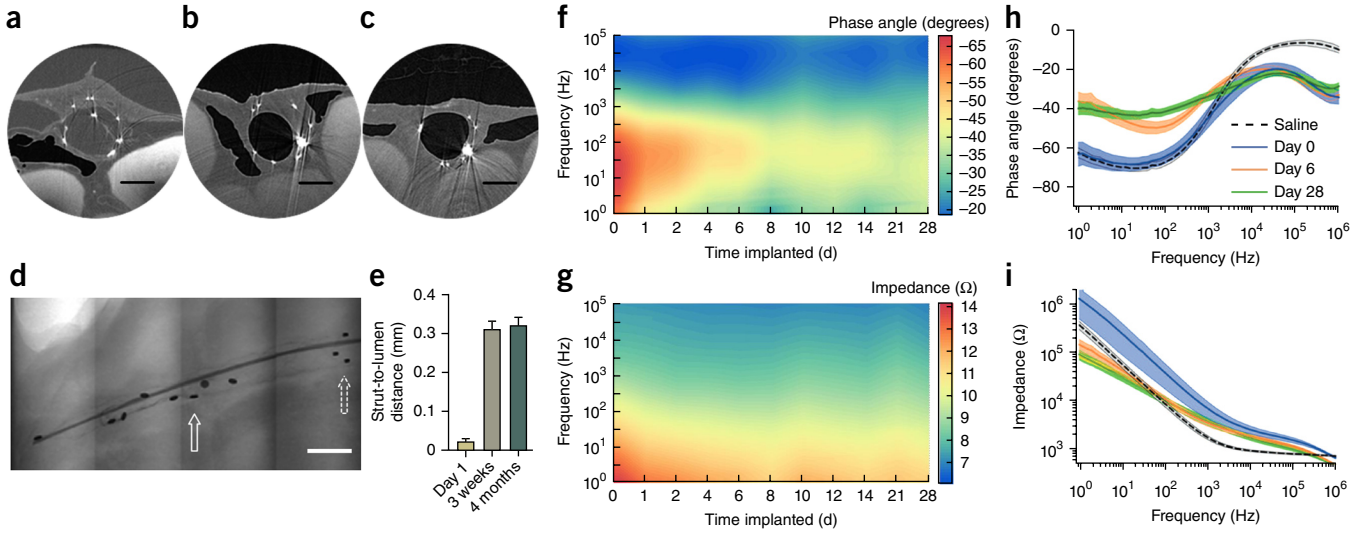

Figure 3 Stentrode vessel wall integration and electrochemical impedance spectroscopy. (**a**–**c**) High-resolution *ex vivo* synchrotron X-ray images of time-dependent vessel wall incorporation of stentrode struts at day 0 (**a**; n = 2 sheep), three weeks (**b**; n = 4 sheep) and four months (**c**; n = 4 sheep) after implantation in superior sagittal sinus. Scale bars, 2 mm. (**d**) Low-resolution image of stentrode after implantation. White arrow shows recording electrodes; dashed arrow shows three proximal markers on expanded stent. Scale bar, 5 mm. (**e**) Synchrotron measured strut-to-lumen distance over the period of implantation (mean ± s.e.m.) (n = 216 struts; 8 sheep). (**f**,**g**) Phase angle (**f**) and impedance magnitude (**g**) changes across a 28-d implantation period. Low-frequency capacitive phase changes over the initial 6 d (100 Hz, one-way ANOVA, $P < 0.0001$). (**h**,**i**) Phase angle (**h**) and impedance measurements (**i**) (mean ± 95% confidence interval; CI) in saline (n = 39) and after implantation at 0 d (n = 28), 6 d (n = 45) and 28 d (n = 33).

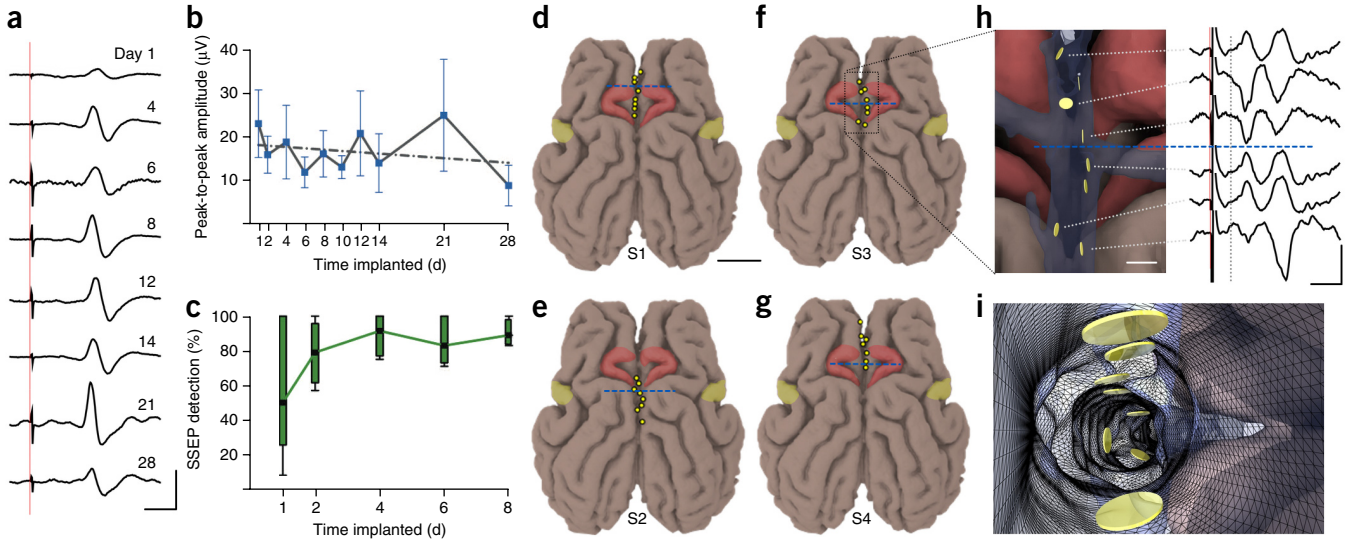

Figure 4 Vascular electrocorticography: somatosensory evoked potentials. (**a**) Representative example of peak-to-peak amplitude over post-implant time (S4). Scale bars, 30 ms and 100 μV. (**b**) Peak-to-peak amplitudes over time (linear regression, $P = 0.42$, $n = 703$ peaks; 5 sheep). (**c**) Detection of SSEPs over early implantation period (box and whisker plot, $n = 5$ sheep). (**d**–**g**) Electrode positions in four sheep implanted with stentrode, demonstrated with co-registered MRI-CT reconstructions to limb motor (red) and sensory (yellow) areas. Scale bar, 2 cm. (**h**,**i**) Three-dimensional reconstructed electrodes within co-registered SSS. Scale bar, 3 mm. Representative variable SSEP morphology with phase reversal dipole (blue dashed line). Scale bars, 30 ms and 50 μV.

between the endovascular, epidural, or subdural arrays. In the higher-power bands (mid gamma to high gamma) a significant difference between the subdural and vascular recordings ($P < 0.01$) was revealed, but not between stentrode and epidural arrays. With regard to the maximum bandwidth, we found a significant difference between stentrode (189 ± 6 Hz (mean ± s.e.), $n = 33$) and subdural (227 ± 7 Hz, one-way ANOVA $P < 0.001$) ECoG recordings, although we found no significant difference between vascular and epidural ECoG recordings (200 ± 6 Hz, one-way ANOVA $P = 0.66$). Our findings therefore demonstrate that the performance of the stentrode is similar to that of an epidural array and marginally inferior to that of a subdural array.

During recording sessions we observed artifacts resulting from chewing muscle activity (chewing artifacts), which have previously been reported as potential impediments to neural decoding, in epidural and subdural recordings[36]. To quantify the effect of chewing artifacts between arrays, we compared the artifact-to-baseline ratio using the root mean square (r.m.s.) of each recording. We observed

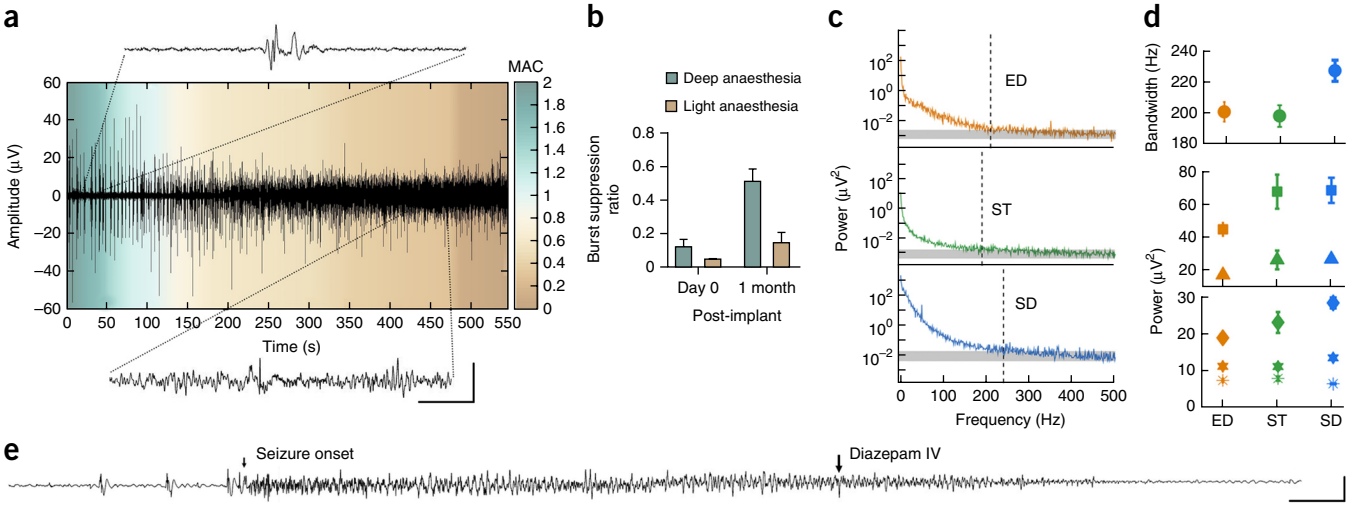

Figure 5 Vascular electrocorticography: endogenous activity. (**a**) Raw vascular electrocorticography of theta burst-suppression in deep (green, isoflurane mean alveolar concentration (MAC) ≥ 1.5) transitioning to light anesthesia (amber, (MAC) ≤ 1). Scale bars, 0.5 s and 50 μV. (**b**) Effect of duration of implantation on detection of burst-suppression (two-way ANOVA, $F_{1,8} = 1\ 2.2$, $P = 0.008$, $n = 5$). (**c**) Representative frequency spectra from subdural (SD), epidural (ED) and stentrode (ST) recordings, displaying characteristic ($1/f$) decrease in the power. Dashed vertical lines indicate maximal bandwidth. (**d**) Maximum bandwidth (top) and spectral content in power bands mu and beta (square and triangle, respectively; middle) and power band gamma (low gamma, diamond; mid gamma, hexagon; high gamma, asterisk; bottom). Error bars show s.e.m. Maximum bandwidth of the stentrode ($n = 41$ electrodes; 8 sheep) was significantly different compared to subdural arrays ($n = 25$ electrodes; 5 sheep, one-way ANOVA $P < 0.001$) but not epidural arrays ($n = 44$ electrodes; 3 sheep, one-way ANOVA $P > 0.5$). (**e**) Raw vascular electrocorticography trace of epileptic seizure in one pilot subject, terminated with intravenous diazepam. Scale bars, 5 s and 200 μV.

© 2016 Nature America, Inc. All rights reserved.

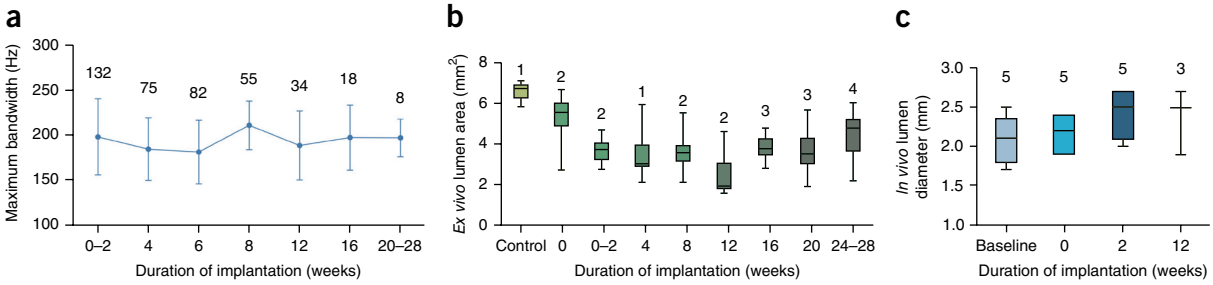

Figure 6 Chronic viability of implanted stentrode. (**a**) Maximum observable bandwidth from recordings (mean ± s.d.). Number of channels per group (n) is indicated in the graph, measured from a total of 10 sheep implanted with a stentrode within the SSS overlying the motor cortex for up to 190 d. (**b**) *Ex vivo* SSS lumen areas. Boxplots indicate the median (line), interquartile range (box) and range (whiskers) Number of sheep per plotted subset is indicated above each box, total $n = 20$ sheep) assessed using synchrotron imaging in 1 mm slices. Control subset is indicative of lumen area from a sheep that was not implanted. (**c**) *In vivo* SSS internal lumen diameter measurements with cerebral angiography after stentrode implantation (2.1 mm median and 1.8–2.4 mm IQR), at day 0 after stentrode implantation (2.2 mm median and 1.9–2.4 mm IQR, $n = 5$ sheep) to two weeks (2.5 mm median and 2.1–2.7 mm IQR, $n = 5$ sheep) or 12 weeks (2.5 mm median and 1.9–2.7 IQR, $n = 3$ sheep).

© 2016 Nature America, Inc. All rights reserved.

no significant differences between the chewing artifacts in the subdural array, epidural array or stentrode (**Supplementary Fig. 12** and **Supplementary Note 5**).

Spectral content, bandwidth and muscle artifact are important parameters that limit the utility of decoding algorithms in chronic telemetry recordings systems. Although signal attenuation has been reported in epidural ECoG recording systems when compared with subdural ECoG[37], signal feature detection may not be adversely affected[38]. We found the spectral content and bandwidth of the stentrode to be similar to those in epidural recordings, but attenuated with respect to those in subdural recordings. We propose that electrode position within a blood vessel, when incorporated into the vessel wall, does not further attenuate signal beyond that explained by the effect of the dura.

In addition, one sheep in the pilot cohort developed unexpected generalized whole-body convulsions 16 h following implantation. A vascular electrocorticography recording from the implanted stentrode clearly illustrated the electrophysiological features of an epileptic seizure, which we terminated with intravenous injection of diazepam (**Fig. 5**).

Chronic viability

We investigated the chronic viability of the stentrode by assessing changes in bandwidth and SSS internal lumen patency over a period of implantation of up to 190 d. To test the capability to reliably record neural signals chronically, we calculated the maximum bandwidth from recordings of resting EEG from each recording electrode in a cohort of 10 sheep (**Supplementary Table 6**). The maximum bandwidth was stable up to 190 d: 197.4 ± 42.0 Hz (mean ± s.d.; $n = 132$) for 0–2 weeks and 196.4 ± 20.7 Hz ($n = 8$) for longer than 20 weeks (**Fig. 6**).

To test the long term patency of venous drainage in the vicinity of the implant, we performed repeated *in vivo* SSS lumen diameter measurements using cerebral angiography up to 12 weeks, then used *ex vivo* synchrotron imaging to evaluate SSS lumen areas after killing the sheep. To minimize thrombosis, we medicated the sheep with daily antiplatelet therapy (aspirin, 100 mg). There was no observed reduction of *in vivo* assessed SSS lumen diameters up to 12 weeks (**Fig. 6**). Cortical veins that entered the SSS at the point of stentrode implantation were open immediately after implant, with 92% (11/12) open two weeks after implant and 63% (5/8) open after three months. None of the sheep with occluded cortical veins demonstrated clinical sequelae such as reduced feeding, difficulty walking or focal neurological signs. Literature on chronic venous thrombosis and occlusion after cardiac pacemaker lead implantation indicates that collateral venous channels emerge, rerouting blood flow around the occlusion[39]. *Ex vivo* assessments using synchrotron X-ray images from 20 sheep implanted for up to 190 d confirmed the patency of the SSS at the stentrode implantation site. We observed SSS lumen area of 4.77 mm^2 (median (2.19–6.03 mm^2 range), $n = 78$ slices from 4 sheep) in animals implanted for longer than 20 weeks (**Fig. 6**).

DISCUSSION

We report the development of an intracranial stentrode array, deployed via minimally invasive catheter angiography in a cerebral vein to achieve chronic recordings in freely moving sheep for up to 190 d. Early incorporation of the stentrode into the vessel wall was associated with an improvement in recording sensitivity.

An endovascular neural interface does not require craniotomy for implantation and may facilitate access to superficial as well as deep brain targets. Our sheep angiography model used the network of superficial veins and sinuses that lie adjacent to areas of cortical surface, with blood vessel internal lumen diameters of 1.2–3.2 mm. We report the use of a delivery method that can deploy a stentrode in vessels as small as 1.7 mm. Although we focused on the veins in the human brain as potential translational target in superficial cortex, the arterial system may also provide an avenue to targeting deep brain structures. Deep structures including the nucleus accumbens and subgenual white matter are known to lie immediately adjacent to the anterior cerebral artery, with a diameter of 1.9–2.6 mm[40]. Other structures not currently targetable without craniotomy, which may be accessible via deep arteries in the human brain include the subthalamic nucleus, hippocampus and internal capsule.

A stentrode that provides intracranial recordings with spatial resolution and spectral content similar to that of an epidural array may facilitate a range of clinical applications. The ideal location of sinuses and cerebral veins overlying superficial cortex may make them natural targets for placement of passive endovascular sensors in a brain-machine interface or epilepsy telemetry recording system. Avoiding direct contact with cortical neurons may mitigate brain trauma and chronic local inflammation, but this requires additional evaluation. Stentrode delivery to a venous sinus may be the safest initial target in humans, owing to the established technical precedence in the form of transverse sinus stenting[41]. However, we propose that the cortical veins are higher-yield targets, with greater exposure to cortical surface and no dural layer that may cause signal attenuation[38].

A current limitation of this prototype technology is the durability of the delivery wire for the stentrode. The device was built on stentriever technology that was not designed for chronic implantation, and we observed wire fatigue associated with repetitive neck movement. Future approaches may borrow from solutions used for cardiac pacemakers, where the issue of chronic repetitive wire fatigue has been overcome[42]. A potentially safer alternative would involve a wireless signal and power transmission system, but currently available technology[43,44] remains too large for safe endovascular deposition. Another limitation is the density of electrodes in the stentrode. The achievable density of recording electrodes might be increased with the removal of electrode wires (wireless), the use of smaller electrodes or with custom-designed stent technology. Further investigation is required to determine the maximum electrode sensitivity and spatial resolution with a stentrode incorporated in the blood vessel.

An endovascular neural interface offers a method for safe, reliable and chronic neural recordings. Just as interventional cardiology progressed into electrophysiological applications after the demonstration of the long-term safety of electrode deposition in veins, which has led to major therapeutic advances that included artificial cardiac pacemakers[22], we envisage that future applications of endovascular arrays may include motor cortex sensors in brain-machine interfaces and seizure prediction in epilepsy. Applications in neural stimulation open the possibility of achieving deep and superficial brain stimulation therapies without the requirement for craniotomy. Multiple deep brain stimulation targets have been identified as being accessible via arteries and veins, with targets for Parkinson's disease and obsessive-compulsive disorder being particularly suitable[40].

METHODS

Methods and any associated references are available in the online version of the paper.

Note: Any Supplementary Information and Source Data files are available in the online version of the paper.

ACKNOWLEDGMENTS

The research was supported by US Defense Advanced Research Projects Agency (DARPA) Microsystems Technology Office contract N66001-12-1-4045; Office of Naval Research (ONR) Global N62909-14-1-N020; National Health and Medical Research Council of Australia (NHMRC) Project Grant APP1062532 and Development Grant APP1075117; Defence Health Foundation, Australia (Booster Grant); Defence Science Institute, Australia, grant; Brain Foundation, Australia, research gift; and the Victorian Government's Operational Infrastructure Support Program. T.J.O. acknowledges the support of the Royal Melbourne Hospital Neuroscience Foundation for the Warren Haynes Fellowship, as well as the Faculty of Medicine, University of Melbourne for the Leslie Eric Paddle Scholarship in Neurology. We thank Covidien (Medtronic) for provision of 30 Solitaire stentriever devices as a product research grant, K. Wilson and S. Cudennec for MRI data acquisition; C. Hall, A. Stevenson and A. Maksimenko for synchrotron acquisition; G. Sharma and S. Salinas for imaging analysis; H. Lau and T. Vale for surgical assistance; and L. Warne for anesthetic assistance. We acknowledge the facilities, and the scientific and technical assistance of the Australian National Imaging Facility at the Melbourne Brain Centre Imaging Unit, as well as the Imaging and Medical beamline at the Australian Synchrotron, Victoria, Australia.

AUTHOR CONTRIBUTIONS

T.J.O., N.L.O., S.E.J., G.S.R., S.M.R., T.L.W., J.W.J., E.H.L., S.H.B, P.P., C.R.F., P.M.D., M.K.H., S.P., A.N.B., D.B.G., C.N.M. and T.J.O'B. designed the experiments. T.J.O., N.L.O., S.E.J., G.S.R., S.M.R., A.J.M., A.D., T.J.H.L., C.S., D.J.G., B.A.M., E.H.L., N.Y., B.C.V.C., Y.T.W., K.E.F., E.S.N., I.E.B., S.H.B., K.A.L., N.R.v.d.N., A.A., K.P.G., B.Y., L.C., L.K., A.N.B., P.J.M., D.B.G., C.N.M. and T.J.O'B. performed the experiments and analysis. T.J.O., N.L.O., S.E.J., G.S.R., S.M.R., T.L.W., L.C., S.M.D., A.N.B., P.J.M., D.B.G. and C.N.M. wrote the paper.

COMPETING FINANCIAL INTERESTS

The authors declare competing financial interests: details are available in the online version of the paper.

Reprints and permissions information is available online at http://www.nature.com/reprints/index.html.

1. Deuschl, G. *et al.* A randomized trial of deep-brain stimulation for Parkinson's disease. *N. Engl. J. Med.* **355**, 896–908 (2006).
2. Mallet, L. *et al.* Subthalamic nucleus stimulation in severe obsessive-compulsive disorder. *N. Engl. J. Med.* **359**, 2121–2134 (2008).
3. Wilson, B.S. *et al.* Better speech recognition with cochlear implants. *Nature* **352**, 236–238 (1991).
4. Weiland, J.D., Cho, A.K. & Humayun, M.S. Retinal prostheses: current clinical results and future needs. *Ophthalmology* **118**, 2227–2237 (2011).
5. Hochberg, L.R. *et al.* Reach and grasp by people with tetraplegia using a neurally controlled robotic arm. *Nature* **485**, 372–375 (2012).
6. Morrell, M.J. Responsive cortical stimulation for the treatment of medically intractable partial epilepsy. *Neurology* **77**, 1295–1304 (2011).
7. Cook, M.J. *et al.* Prediction of seizure likelihood with a long-term, implanted seizure advisory system in patients with drug-resistant epilepsy: a first-in-man study. *Lancet Neurol.* **12**, 563–571 (2013).
8. Hochberg, L.R. *et al.* Neuronal ensemble control of prosthetic devices by a human with tetraplegia. *Nature* **442**, 164–171 (2006).
9. Yanagisawa, T. *et al.* Electrocorticographic control of a prosthetic arm in paralyzed patients. *Ann. Neurol.* **71**, 353–361 (2012).
10. Wang, W. *et al.* An electrocorticographic brain interface in an individual with tetraplegia. *PLoS One* **8**, e55344 (2013).
11. Polikov, V.S., Tresco, P.A. & Reichert, W.M. Response of brain tissue to chronically implanted neural electrodes. *J. Neurosci. Methods* **148**, 1–18 (2005).
12. Karumbaiah, L. *et al.* Relationship between intracortical electrode design and chronic recording function. *Biomaterials* **34**, 8061–8074 (2013).
13. Saxena, T. *et al.* The impact of chronic blood-brain barrier breach on intracortical electrode function. *Biomaterials* **34**, 4703–4713 (2013).
14. Yanagisawa, T. *et al.* Neural decoding using gyral and intrasulcal electrocorticograms. *Neuroimage* **45**, 1099–1106 (2009).
15. Driller, J. *et al.* Development and use of the POD catheter in the cerebral vascular system. *Med. Res. Eng.* **8**, 11–16 (1969).
16. Penn, R.D., Hilal, S.K., Michelsen, W.J., Goldensohn, E.S. & Driller, J. Intravascular intracranial EEG recording. Technical note. *J. Neurosurg.* **38**, 239–243 (1973).
17. Boniface, S.J. & Antoun, N. Endovascular electroencephalography: the technique and its application during carotid amytal assessment. *J. Neurol. Neurosurg. Psychiatry* **62**, 193–195 (1997).
18. Bower, M.R. *et al.* Intravenous recording of intracranial, broadband EEG. *J. Neurosci. Methods* **214**, 21–26 (2013).
19. Mikuni, N. *et al.* "Cavernous sinus EEG": a new method for the preoperative evaluation of temporal lobe epilepsy. *Epilepsia* **38**, 472–482 (1997).
20. Watanabe, H., Takahashi, H., Nakao, M., Walton, K. & Llinás, R.R. Intravascular neural interface with nanowire electrode. *Electron. Commun. Jpn.* **92**, 29–37 (2009).
21. Furman, S. & Schwedel, J.B. An intracardiac pacemaker for Stokes-Adams seizures. *N. Engl. J. Med.* **261**, 943–948 (1959).
22. Mirowski, M. *et al.* Termination of malignant ventricular arrhythmias with an implanted automatic defibrillator in human beings. *N. Engl. J. Med.* **303**, 322–324 (1980).
23. Chimowitz, M.I. *et al.* Stenting versus aggressive medical therapy for intracranial arterial stenosis. *N. Engl. J. Med.* **365**, 993–1003 (2011).
24. Puffer, R.C., Mustafa, W. & Lanzino, G. Venous sinus stenting for idiopathic intracranial hypertension: a review of the literature. *J. Neurointerv. Surg.* **5**, 483–486 (2013).
25. Berkhemer, O.A. *et al.* A randomized trial of intraarterial treatment for acute ischemic stroke. *N. Engl. J. Med.* **372**, 11–20 (2015).
26. Campbell, B.C.V. *et al.* Endovascular therapy for ischemic stroke with perfusion-imaging selection. *N. Engl. J. Med.* **372**, 1009–1018 (2015).
27. Hoffmann, A. *et al.* The ovine cerebral venous system: comparative anatomy, visualization, and implications for translational research. *PLoS One* **9**, e92990 (2014).
28. Shao, Y., Sun, J.-L., Yang, Y., Cui, Q.-K. & Zhang, Q.-L. Endoscopic and microscopic anatomy of the superior sagittal sinus and torcular herophili. *J. Clin. Neurosci.* **16**, 421–424 (2009).
29. Van Belle, E. *et al.* Stent endothelialization. Time course, impact of local catheter delivery, feasibility of recombinant protein administration, and response to cytokine expedition. *Circulation* **95**, 438–448 (1997).
30. van der Giessen, W.J. *et al.* Coronary stenting with a new, radiopaque, balloon-expandable endoprosthesis in pigs. *Circulation* **83**, 1788–1798 (1991).
31. Franks, W., Schenker, I., Schmutz, P. & Hierlemann, A. Impedance characterization and modeling of electrodes for biomedical applications. *IEEE Trans. Biomed. Eng.* **52**, 1295–1302 (2005).
32. Henle, C. *et al.* First long term *in vivo* study on subdurally implanted micro-ECoG electrodes, manufactured with a novel laser technology. *Biomed. Microdevices* **13**, 59–68 (2011).
33. Cedzich, C., Taniguchi, M., Schäfer, S. & Schramm, J. Somatosensory evoked potential phase reversal and direct motor cortex stimulation during surgery in and around the central region. *Neurosurgery* **38**, 962–970 (1996).
34. Allison, T. *et al.* Human cortical potentials evoked by stimulation of the median nerve. I. Cytoarchitectonic areas generating short-latency activity. *J. Neurophysiol.* **62**, 694–710 (1989).

© 2016 Nature America, Inc. All rights reserved.

35. Lukatch, H.S., Kiddoo, C.E. & Maciver, M.B. Anesthetic-induced burst suppression EEG activity requires glutamate-mediated excitatory synaptic transmission. *Cereb. Cortex* **15**, 1322–1331 (2005).
36. Shimoda, K., Nagasaka, Y., Chao, Z.C. & Fujii, N. Decoding continuous three-dimensional hand trajectories from epidural electrocorticographic signals in Japanese macaques. *J. Neural Eng.* **9**, 036015 (2012).
37. Bundy, D.T. *et al.* Characterization of the effects of the human dura on macro- and micro-electrocorticographic recordings. *J. Neural Eng.* **11**, 016006 (2014).
38. Torres Valderrama, A., Oostenveld, R., Vansteensel, M.J., Huiskamp, G.M. & Ramsey, N.F. Gain of the human dura *in vivo* and its effects on invasive brain signal feature detection. *J. Neurosci. Methods* **187**, 270–279 (2010).
39. Stoney, W.S. *et al.* The incidence of venous thrombosis following long-term transvenous pacing. *Ann. Thorac. Surg.* **22**, 166–170 (1976).
40. Teplitzky, B.A., Connolly, A.T., Bajwa, J.A. & Johnson, M.D. Computational modeling of an endovascular approach to deep brain stimulation. *J. Neural Eng.* **11**, 026011–026014 (2014).
41. Ahmed, R.M. *et al.* Transverse sinus stenting for idiopathic intracranial hypertension: a review of 52 patients and of model predictions. *AJNR Am. J. Neuroradiol.* **32**, 1408–1414 (2011).
42. Fortescue, E.B. *et al.* Patient, procedural, and hardware factors associated with pacemaker lead failures in pediatrics and congenital heart disease. *Heart Rhythm* **1**, 150–159 (2004).
43. Ho, J.S. *et al.* Wireless power transfer to deep-tissue microimplants. *Proc. Natl. Acad. Sci. USA* **111**, 7974–7979 (2014).
44. Muller, R. *et al.* A miniaturized 64-channel 225μW wireless electrocorticographic neural sensor. *2014 IEEE International Solid-State Circuits Conference (ISSCC)* 412–413 (IEEE, 2014).

© 2016 Nature America, Inc. All rights reserved.

ONLINE METHODS

Human cerebral veins and cortical surface. 50 consecutive post-contrast 1.5 T (Sigma, GE) MRI venogram fast spoiled gradient echo sequences of brain[45] performed for suspected venous sinus thrombosis (median age 34.5, range 18–73) but reported as normal by a neuroradiologist, were retrospectively assessed. Field of view was 220 mm × 176 mm, slice thickness was 1.4 mm (voxel size, 0.6 mm × 0.8 mm × 1.4 mm), flip angle 20°, variable minimum TR/TE, NEX 1 (time repetition/time echo, number of excitations). A neurologist (T.O.) performed manual identification of superficial cerebral veins using the 3DSlicer toolkit[46]. Cortical veins greater than 2 mm in diameter and running in the corresponding sulcus were classified as preCSV, CSV or postCSV. To determine vessel lumen diameters and proximity to sensorimotor cortex, fiducial points were manually allocated along the pathway of the veins and SSS in 5-mm increments distally (**Supplementary Fig. 1**). The first fiducial point for the SSS was placed at the intersection with the post-central sulcus, and for the cortical veins, at the point of joining the SSS. Sinus and vein diameters were manually measured at each fiducial point, manipulating multiplanar images to achieve both longitudinal and cross-sectional view of the vein[47]. The narrowest diameter measurement from each plane was taken. Cortical segmentation and labeling of primary motor cortex (Brodmann area 4, BA4) and primary sensory cortex (Brodmann area 1, BA1) were performed for each subject[48,49] using the FreeSurfer software suite (http://surfer.nmr.mgh.harvard.edu). The distance from each fiducial point within each blood vessel to the nearest BA4 and BA1 cortical surface was measured manually. A distance of less than 2 mm was presumed to be zero due to measurement error limited by voxel resolution in FreeSurfer. Surface mesh from internal vein lumens were reconstructed using the VMTK module (http://www.vmtk.org)[50] in the 3DSlicer toolkit (http://www.slicer.org)[46] and co-registered using FreeSurfer (**Fig. 1**).

Sheep cerebral veins and cortical surface. 13 consecutive post-contrast 1.5 T brain MRI scan (Sigma) venogram fast spoiled gradient echo sequences[45] were acquired in Corriedale sheep under general anesthesia with thiopentone for induction and isoflurane for maintenance. Field of view was 180 mm × 180 mm, slice thickness 1 mm, flip angle 20°, NEX 1. Vein diameters were measured from the external jugular vein to cortical veins. Fiducial points in SSS were allocated in 5-mm increments, commencing at the bifurcation of transverse sinuses in an anterior direction using the 3DSlicer toolkit. The SSS was reconstructed using the VMTK module in 3DSlicer from the contrast-enhanced MRI images, for visual inspection and surgical planning for angiography. The motor cortex was defined as the superior frontal gyrus[51–53]. Distances from cortical surface of the left and right motor area in the superior frontal gyrus were measured at each fiducial point (**Supplementary Note 6**). The forelimb area of the sensory cortex was defined as the border of the anterior suprasylvian sulcus and the cruciate sulcus (**Fig. 4**)[54].

Stentrode fabrication. Self-expanding stentrodes were fabricated by mounting electrodes on commercially available Nitinol stents (Solitaire SAB, Covidien) using a biocompatible, ultraviolet curable adhesive (Dymax, 1128A-M, UV Pacific). Stent heads with a nominal length of 31.1 mm and expanded diameter of 3.0 mm were secured in a reversed orientation on a 310 µm diameter stainless steel shaft insulated with 0.025-inch thick walled heat shrink (01030433, Vention Medical). Platinum (Goodfellow) disc electrodes (50 µm thickness, 750 µm diameter) were resistance-welded (UB25, Muyachi Unitek) to 25-µm diameter (+6 µm polyimide insulation) 92% platinum and 8% tungsten wire (Goodfellow). Electrodes were mounted on stent struts using ultraviolet light–curable adhesive, with electrode wires wrapped around the stent lattice structure. Wires were wound around the stent shaft using a length of ~40 cm and wrapped around 5-mm sections of silicone tube with an external diameter of 640 µm (Silastic, Dow Corning) and connected to platinum tubes (3 mm length, 787 µm internal diameter, 878 µm external diameter; Johnson Matthey) using conductive epoxy (CW2400J, ITW, Chemtronics). The wires and stent shaft were insulated using 0.033-inch thin walled heat shrink (033025CST, Vention Medical).

Sheep catheter venography. A catheter technique to navigate into distal cerebral veins was developed in a sheep model. Cerebral angiography was performed on animals under approval of the Florey Institute of Neuroscience and Mental Health, Animal Ethics Committee, project 11-055. Puncture was performed at the external jugular vein following surgical cut down in the neck, at a position one-third the distance between the angle of the mandible and the clavicle. Access was secured using the Seldinger technique (0.035-inch, Safe-T-J Curved Wire, Cook Medical) with an 6F sheath (0.088-inch inner diameter, NeuronMax, Penumbra). An intravenous heparin bolus of 150 units/kg was given post puncture, and activated clotting time (ACT) measured at half-hour intervals (ACT Plus, Medtronic). Additional boluses of 2,000 units of heparin were given when ACT < 250 s. Digital subtraction angiography with road-mapping (Arcadis Avantic, Siemens) of the venous pathway was used to navigate the microwire and catheters to the target vessel using radio-opaque contrast (Omnipaque 240, GE Healthcare).

The venous pathway to SSS from external jugular vein contained three venous convergences that required coaxial catheter telescopic navigation: (i) the convergence of the external jugular vein with the maxillary vein at the level of the angle of the mandible[27], which was negotiated with a microcatheter-over-microwire technique; (ii) negotiating the maxillary vein as it entered the skull at the jugular foramen, forming the temporal sinus, and converging with the transverse sinus; and (iii) negotiating the confluence of sinuses formed by the convergence of superior and inferior sagittal sinuses with transverse sinus. Forming a 'J' shape to the distal tip of the microwire (**Supplementary Fig. 5**) in combination with advancement of 45° shaped 2F microcatheter, was effective at navigating irregular venous anatomy that includes valves and chordae[27]. To achieve catheter access into the confluence of sinuses, all catheters (including 6F sheath) were telescoped up the maxillary vein to sit flush at the commencement of the temporal sinus. A digital subtraction contrast run was performed to create a roadmap of the confluence of sinuses and SSS. To enable entry into the SSS, a loop was created in the leading microwire, by pressing against the posterior wall of the confluence of sinuses. The microcatheter was fed over the microwire, and advanced distally into the SSS leading with the atraumatic microwire loop. Advancing the 4F catheter through the confluence of sinuses required positioning of the 6F catheter at the base of confluence of sinuses. The 4F catheter was then fed into the sinus using a gentle grinding technique (slow push and twist) over the microcatheter. The stentrode was fed through the 4F catheter, which was then retracted to unsheathe the array into the target location in the SSS. A contrast run was performed to assess flow through the stentrode immediately post deployment. Vessel closure was performed at the vein puncture with purse string suture around the stentrode shaft.

Data acquisition. *Signal recording.* Signal was recorded using a 32-channel digital DC common average reference amplifier (TMSi Porti, Twente Medical Systems International). The recordings were sampled at 2,048 Hz, with the average of all connected channels used as the reference. The amplifier did not require any external referencing, and no hardware filtering was used. The ground electrode was either a platinum plate placed under the skin on the skull or a stainless steel plate placed under the skin on the back (**Supplementary Fig. 8**). Preliminary analysis of the data showed that there was no difference in the signal obtained using the different ground electrodes. Data were stored using Matlab scripts (MathWorks) and the FieldTrip toolbox14 (ref. 55).

Animal cohorts. The lowest number of animals required to demonstrate feasibility was used in accordance with the policy of the institutional animal ethics committee and National Health and Medical Research Council (NHMRC) recommendations. Complex signal acquisition was acquired in a consecutive cohort following stentrode implantation in five Corriedale female sheep for a prespecified period of three months, for the measurement of vessel patency, impedance, SSEP and anesthesia modulation signal recording (see below). A further cohort of seven sheep with stentrode implantation was used to record resting ECoG for intracranial surface array validation and impedance measurements (see below). To demonstrate chronic viability, a cohort of ten sheep was included for assessment of resting EEG and 20 sheep were assessed with *ex vivo* synchrotron imaging at variable time points post implantation to examine changes in internal lumen area in a period up to 190 d.

Vessel patency. In vivo assessments of venous patency were assessed in a cohort of five sheep with repeated diagnostic cerebral angiography performed at baseline (day 0), two weeks and 12 weeks following successful stentrode implantation. Baseline venography involved direct venous contrast injections

© 2016 Nature America, Inc. All rights reserved.

immediately before deployment. Follow-up angiograms involved arterial injections and venous phase image capture. Cortical veins draining into the SSS through the stent struts of the implanted stentrode were identified by an interventional neuroradiologist (P.M.) and confirmed by a vascular neurologist (B.C.) in the baseline implantation images. Veins were classified as either patent or occluded at two week and three month catheter angiograms with visual confirmation of blood flow. The diameter of the internal lumen of the vessel at the midpoint of the stentrode was also measured. *Ex vivo* synchrotron X-ray imaging was used to assess blood vessel patency at four-week intervals of stentrode implantation up to 190 d.

Synchrotron imaging. *Acquisition*. To enable assessment of incorporation of the stentrode into the vessel wall tissue over time and comparison with changes in electrical impedance spectroscopy, images of *ex vivo* brains with implanted stentrodes at day 1 (n = 2), 3 weeks (mean 21 d (range 9–34 d); n = 4) and four months (mean 139 d (range 98–182 d), n = 4) were captured noninvasively using a synchrotron X-ray. For assessment of chronic viability, a 20 animal cohort was assessed *ex vivo* at four week intervals for up to 190 d (**Supplementary Table 5**). Immediately after animals were euthanized brain tissue and vessel fixation was performed with bilateral carotid artery infusion of 10% formaldehyde. The skull was carefully removed from brain, leaving dura, sinuses and implanted stentrode intact. Samples were stored in 4% paraformaldehyde. Prior to imaging, tissues were immersed in Lugol's solution (5% wt/vol iodine, 10% wt/vol potassium iodine; Complementary Components) for 96 h[56]. Images were acquired at the imaging and medical beamline (IMBL) of the 3.0 GeV Australian Synchrotron with a 136 m source-to-sample distance. Samples were scanned at 50 KeV using a Ruby detector (4Dx, Melbourne, Australia) with a 25-µm-thick scintillator and sample-to-detector distance of 1,000 mm (0.4 s exposure). 1,800 images (13.75–50 µm pixel resolutions) were taken as the sample was rotated around 180°, with an additional 20 darkfield and lightfield frames taken for image correction[57]. Sequential 10-mm sample window z scans (with 2.5 mm overlap) were required to scan the entire sample. Example high (13.75 µm pixel) and low (50 µm pixel) resolution images are shown in **Figure 3**. Images were reconstructed using XTRACT (MASSIVE CWSx64, Version 8.1.2.6829M, CSIRO) to form sequential z stacks, which were imported into ImageJ (1.48i, US National Institutes of Health) for analysis.

Analysis. Stentrode incorporation into vessel wall was quantified by measuring strut-to-lumen distance[58] in multiple high-resolution slices (6, range 4–9) per stentrode. Slices were taken at inter-electrode positions along the stentrode to minimize artifact caused by discs. Strut measurements were taken from the center of the strut to minimize error related to blooming artifact[59]. Lumen was defined as a congruent area of reduced density with respect to the surrounding vessel wall and dura (**Fig. 3**). Lumen area was measured using digital morphometry[58] from slices (median, 20 slides; range, 19–29 slices; n = 20 animals) at 1-mm intervals from the distal to proximal ends of the stentrode.

Impedance. Full-spectrum electrochemical impedance spectroscopy (5 mV sinusoidal pulse, 1 Hz to 100 kHz, 10 points per decade) was measured for each of the electrodes before implantation, and after implantation on alternate days for two weeks, and weekly thereafter using a Gamry Z100 potentiostat (Interface 1000). For *in vivo* recordings, electrodes were referenced to a custom-made, 55.2 mm^2 U-shaped platinum-foil, unidirectional ground electrode that was implanted subcutaneously in the scalp. To ensure a well-defined surface, electrodes were cleaned before implantation by voltammetry cycling, from −1.5 V to 1.5 V with a scan rate of 500 mV/s for typically 20–40 cycles until the measurements stabilized[31]. Impedance measurements were taken using a two-electrode configuration[60] and performed in a saline (0.9% NaCl) bath before implantation. A minimum of three recordings were taken for each measurement and averaged.

Somatosensory evoked potentials. SSEPs were measured over time in a cohort of sheep (n = 5) after implantation of the stentrode. SSEPs were recorded (alternate days for two weeks, then weekly) on awake, mobile and resting sheep in an individual pen, with no restriction on their posture or movement. Bipolar electrical stimulation (2 cm interelectrode distance) was delivered through a custom-made strap electrode placed over shaved skin at the location of the forelimb median nerve, 5 cm medial and superior to the elbow joint[61]. Stimulation currents were generated using an AMPI Master-8 connected to a constant stimulus isolator AMPI Iso-flex. Minimal suprathreshold stimulation current was determined by titrating current of a single 500-µs pulse until a reliable forelimb contraction was visually confirmed[34]. Stimulation was delivered at a frequency of 0.613 Hz for a duration of up to 4 min, generating 147 trials, repeated for left and right forelimbs, aiming to deliver at least three times the number needed to generate SSEPs from known exposed cortical surface recordings (32–48 trials)[34].

Anesthesia modulation. Theta burst-suppression was induced in a portion of the cohort (4 sheep) where feasible, as limited by the safety of duration of the surgical procedure after implantation, at day 0 implantation (2 sheep) and at one month (median of 34 d and range of 14–60 d; 4 sheep), by means of general anesthetic agents known to suppress cortical activity at relatively low dose[35,62,63]. Anesthesia was induced using thiopentone administered intravenously at 15 mg/kg. Orotracheal intubation was performed and the tube connected to a rebreathing system. Anesthesia was maintained using isoflurane in oxygen. End-tidal isoflurane concentration was measured using a side-stream gas analyzer and maintained at 3.2% (equivalent to MAC 2.0; ref. 64) before commencement of vascular electrocorticography recordings. Isoflurane was then weaned, waking up the animal over a 15-min period. Vascular electrocorticography was recorded until the animal regained voluntary motor function.

Seizure recording. In one subject from the pilot cohort, the angiography procedure was complicated by subdural hemorrhage. The subject was successfully recovered postoperatively, but developed persistent whole-body convulsions 16 h following surgery. To confirm the clinical suspicion of epileptic seizures, vascular electrocorticography was recorded before and during administration of 5 mg intravenous diazepam, which resulted in termination of the convulsions (**Fig. 5**). A zero-phase Butterworth bandpass filter was applied to the data from 1 Hz to 200 Hz, as well as a 50 Hz digital notch filter to reduce line noise. Electrophysiological morphology was confirmed as an epileptic seizure by two independent clinical neurophysiologists (T.J.O'B. and L.K.).

Intracranial array validation. To compare spectra and noise floors of the stentrode to commercially available surface ECoG arrays, recordings at rest were obtained from eight sheep. Only sheep with stentrode implantation duration greater than 7 d were included. Sheep were awake and mobile in individual pens, with no restriction on their posture or movement. Craniotomy and array insertion was performed following stentrode implantation. Subdural and epidural arrays were placed over the superior frontal gyrus immediately adjacent to the intravascular array within the SSS. Intraoperative X-ray was used to confirm position of the arrays (**Supplementary Fig. 11**).

Signal analysis. *Somatosensory evoked potentials.* Neural signal was band pass–filtered to between 10 Hz and 1,024 Hz[65] with fourth-order zero-phase Butterworth filters. Each stimulus time-locked epoch SSEP trial (−100 ms to 200 ms) was manually reviewed to exclude major artifact indicated by abnormally high-amplitude waveforms (>200 µV) and then averaged. Averaged SSEP waveforms were manually reviewed by a neurologist (T.J.O.) to determine the latency and corresponding absolute amplitudes of the first four peaks as well as the maximal peak-to-peak amplitudes. SSEP amplitude error was calculated using the prestimulation range for the averaged SSEP waveform, which approached 0 µV for a pure SSEP waveform without background EEG noise. The average error across all experiments was ±2.88 µV, therefore peaks less than 3 µV were rejected from analysis. A clinical neurophysiologist (L.K.) performed a second review to confirm presence, latency and amplitude of all peaks. To quantify physiological distribution, all peaks were rectified, pooled and assessed in a histogram. As a metric of signal stability, the effect of duration of implantation on maximal peak-to-peak amplitude was assessed using a random effect linear regression model. To test the variability in the recorded signal across electrodes, the Pearson's correlation coefficient was calculated between all electrode pairs within an animal. Correlations were calculated over a period of 100 ms before to 200 ms after the stimulus onset. Due to the stability of the signal across days, the coefficients were averaged across all recording sessions.

Anesthesia modulation. ECoG recordings were notch-filtered (50 Hz and harmonics) and band pass–filtered (1–100 Hz) with fourth-order zero-phase Butterworth filters. The data were segmented into 4-s epochs, and classified as deep (≥1.5 MAC) or light (≤1 MAC) anesthesia for analysis. Isoelectric

© 2016 Nature America, Inc. All rights reserved.

doi:10.1038/nbt.3428

segments were identified within each 4 s epoch and averaged within deep and light anesthesia states for each electrode. Burst suppression ratio was calculated as the percentage of a 4-s epoch of raw vascular electrocorticography considered to be isoelectric (≤5 μV amplitude) for greater than 0.5 s[66]. The mean burst suppression ratio of all electrodes was then calculated per animal. A two way ANOVA was performed to assess the effect of duration of implantation and anesthesia state.

Electrocorticography validation. Recordings were notch-filtered (50 Hz and harmonics) and then high pass–filtered (0.5 Hz) with fourth order zero-phase Butterworth filters. The data were segmented into 2-s epochs and a moving root mean square (r.m.s.) was calculated in a 100-ms moving window and compared to the background r.m.s. Artifacts were detected when the moving average crossed a threshold of 4 × baseline r.m.s. and by *post hoc* visual inspection. Artifacts (gross movement and electrical artifact) in the recordings were excluded from further analysis. Thomson's multitaper method was used to estimate the spectral content within each temporal window, and tapered using discrete prolate spheroidal sequences with a spectral concentration of 1 Hz around the center frequency[67]. The noise of each electrode was estimated using the median spectral power between 455 Hz and 495 Hz of each recording electrode[37]. This frequency band was chosen due to being the highest frequency band located below the Nyquist frequency and between any 50-Hz band. Median spectral content in each 10-Hz bin (0.5–512 Hz) was compared to the median of the noise. A 10-Hz bin was considered dissimilar from noise if the median power was greater than the upper boundary of the noise (third quartile plus 1.5 IQR). Because ECoG power spectra are not normally distributed and display substantial within-subject variability, the average power spectrum of each array was normalized to the median noise power and log-transformed. Normalized power spectrums were then compared using independent-samples *t*-test and the agreement across the spectrum was evaluated using Lin's concordance correlation coefficient. To assess chronic viability, maximum bandwidth in resting EEG from each sheep in the cohort was binned into two to four-week bins and the normality of the distributions of maximum bandwidth at each time was verified through visual inspection by the Kolmogorov-Smirnov test.

45. Sun, J., Wang, J., Jie, L., Wang, H. & Gong, X. Visualization of the internal cerebral veins on MR phase-sensitive imaging: comparison with 3D gadolinium-enhanced MR venography and fast-spoiled gradient recalled imaging. *AJNR Am. J. Neuroradiol.* **32**, E191–E193 (2011).
46. Fedorov, A. *et al.* 3D Slicer as an image computing platform for the Quantitative Imaging Network. *Magn. Reson. Imaging* **30**, 1323–1341 (2012).
47. Dill, T. *et al.* Pulmonary vein diameter reduction after radiofrequency catheter ablation for paroxysmal atrial fibrillation evaluated by contrast-enhanced three-dimensional magnetic resonance imaging. *Circulation* **107**, 845–850 (2003).
48. Dale, A.M., Fischl, B. & Sereno, M.I. Cortical surface-based analysis. I. Segmentation and surface reconstruction. *Neuroimage* **9**, 179–194 (1999).
49. Fischl, B., Sereno, M.I. & Dale, A.M. Cortical surface-based analysis. II: Inflation, flattening, and a surface-based coordinate system. *Neuroimage* **9**, 195–207 (1999).
50. Antiga, L. *et al.* An image-based modeling framework for patient-specific computational hemodynamics. *Med. Biol. Eng. Comput.* **46**, 1097–1112 (2008).
51. Bagley, C. Cortical motor mechanism of the sheep brain. *Arch. Neurol. Psychiatry* **7**, 417–453 (1922).
52. Simpson, S. & King, J.L. Localisation of the motor area in the sheep. *Exp. Physiol.* **4**, 53–65 (1911).
53. Grovum, W.L. & Gonzalez, J.S. Electrical stimulation of the medial frontal lobe elicits a pattern of body movements in sheep. *Brain Res.* **851**, 252–253 (1999).
54. Johnson, J.I., Rubel, E.W. & Hatton, G.I. Mechanosensory projections to cerebral cortex of sheep. *J. Comp. Neurol.* **158**, 81–107 (1974).
55. Oostenveld, R., Fries, P., Maris, E. & Schoffelen, J.-M. FieldTrip: open source software for advanced analysis of MEG, EEG, and invasive electrophysiological data. *Comput. Intell. Neurosci.* **2011**, 156869 (2011).
56. Metscher, B.D. MicroCT for comparative morphology: simple staining methods allow high-contrast 3D imaging of diverse non-mineralized animal tissues. *BMC Physiol.* **9**, 11 (2009).
57. Stevenson, A.W. *et al.* First experiments on the Australian Synchrotron Imaging and Medical beamline, including investigations of the effective source size in respect of X-ray imaging. *J. Synchrotron Radiat.* **17**, 75–80 (2010).
58. Morlacchi, S. *et al.* Hemodynamics and in-stent restenosis: micro-CT images, histology, and computer simulations. *Ann. Biomed. Eng.* **39**, 2615–2626 (2011).
59. Nieman, K., Cademartiri, F., Raaijmakers, R., Pattynama, P. & de Feyter, P. Noninvasive angiographic evaluation of coronary stents with multi-slice spiral computed tomography. *Herz* **28**, 136–142 (2003).
60. Williams, J.C., Hippensteel, J.A., Dilgen, J., Shain, W. & Kipke, D.R. Complex impedance spectroscopy for monitoring tissue responses to inserted neural implants. *J. Neural Eng.* **4**, 410–423 (2007).
61. Ghoshal, N.G. & Getty, R. Innervation of the forearm and fin the ox (*Bos taurus*), sheep (*Ovis aries*) and goat (*Capra hircus*). *Iowa State Univ. Vet.* **29**, 19–29 (1967).
62. Ogawa, T., Shingu, K., Shibata, M., Osawa, M. & Mori, K. The divergent actions of volatile anaesthetics on background neuronal activity and reactive capability in the central nervous system in cats. *Can. J. Anaesth.* **39**, 862–872 (1992).
63. Villeneuve, M.Y. & Casanova, C. On the use of isoflurane versus halothane in the study of visual response properties of single cells in the primary visual cortex. *J. Neurosci. Methods* **129**, 19–31 (2003).
64. Palahniuk, R.J., Shnider, S.M. & Eger, E.I. II. Pregnancy decreases the requirement for inhaled anesthetic agents. *Anesthesiology* **41**, 82–83 (1974).
65. Chiappa, K.H. *Evoked Potentials in Clinical Medicine* (Lippincott Williams & Wilkins, 1997).
66. Rampil, I.J. A primer for EEG signal processing in anesthesia. *Anesthesiology* **89**, 980–1002 (1998).
67. Thomson, D.J. Spectrum estimation and harmonic analysis. *Proc. IEEE* **70**, 1055–1096 (1982).

© 2016 Nature America, Inc. All rights reserved.